Journal of ELECTRONIC MATERIALS, Vol. 43, No. 6, 2014
DOI: 10.1007/s11664-013-2865-8

Transport and Mechanical Properties of High-ZT $Mg_{2.08}Si_{0.4-x}Sn_{0.6}Sb_x$ Thermoelectric Materials

PENG GAO,[1] ISIL BERKUN,[2] ROBERT D. SCHMIDT,[1] MATTHEW F. LUZENSKI,[2] XU LU,[3] PATRICIA BORDON SARAC,[1] ELDON D. CASE,[1] and TIMOTHY P. HOGAN[1,2,4]

1.—Department of Chemical Engineering and Materials Science, Michigan State University, East Lansing, MI 48824, USA. 2.—Department of Electrical and Computer Engineering, Michigan State University, East Lansing, MI 48824, USA. 3.—Department of Physics and Astronomy, Michigan State University, East Lansing, MI 48824, USA. 4.—e-mail: hogant@msu.edu

$Mg_2(Si,Sn)$ compounds are promising candidate low-cost, lightweight, nontoxic thermoelectric materials made from abundant elements and are suited for power generation applications in the intermediate temperature range of 600 K to 800 K. Knowledge on the transport and mechanical properties of $Mg_2(Si,Sn)$ compounds is essential to the design of $Mg_2(Si,Sn)$-based thermoelectric devices. In this work, such materials were synthesized using the molten-salt sealing method and were powder processed, followed by pulsed electric sintering densification. A set of $Mg_{2.08}Si_{0.4-x}Sn_{0.6}Sb_x$ ($0 \le x \le 0.072$) compounds were investigated, and a peak ZT of 1.50 was obtained at 716 K in $Mg_{2.08}Si_{0.364}Sn_{0.6}Sb_{0.036}$. The high ZT is attributed to a high electrical conductivity in these samples, possibly caused by a magnesium deficiency in the final product. The mechanical response of the material to stresses is a function of the elastic moduli. The temperature-dependent Young's modulus, shear modulus, bulk modulus, Poisson's ratio, acoustic wave speeds, and acoustic Debye temperature of the undoped $Mg_2(Si,Sn)$ compounds were measured using resonant ultrasound spectroscopy from 295 K to 603 K. In addition, the hardness and fracture toughness were measured at room temperature.

Key words: Thermoelectrics, $Mg_2(Si,Sn)$, transport properties, mechanical properties

INTRODUCTION

The thermoelectric effect is one basic type of solid-state energy conversion in which heat can be directly converted to electricity or heating/cooling can be achieved by applying a current through certain materials without any moving parts involved. An important application of thermoelectrics is collecting waste heat for power generation purposes.[1] It has been predicted that a 10% to 20% increase in fuel economy could be achieved in automobiles by using thermoelectric devices to collect exhaust heat.[2] Radioisotope thermoelectric generators (RTG) have been used in satellites as well as deep-space exploration missions such as the Cassini probe to collect heat from radioactive decay to generate electricity to power electronic devices on board.[3]

The efficiency of thermoelectric energy conversion depends on a material's properties and can be evaluated by the dimensionless figure of merit ZT:

$$ZT = \frac{S^2\sigma}{\kappa}T, \quad (1)$$

where S, σ, and κ are the Seebeck coefficient, electrical conductivity, and thermal conductivity of the material. Generally, $ZT = 1$ is the benchmark for good thermoelectric materials. Materials such as Bi_2Te_3-based ($ZT \approx 1.3$)[4] and PbTe-based ($ZT \approx 2.2$)[5] materials have been found to exhibit excellent thermoelectric properties.

(Received July 8, 2013; accepted October 11, 2013; published online December 10, 2013)

Intensive research has been conducted on $Mg_2(Si,Sn)$-based thermoelectric materials recently, due to their thermoelectric properties, which are comparable to some of the best known thermoelectric materials, the abundance of their constituent elements, and their low mass densities. Commonly, $Mg_2(Si,Sn)$-based thermoelectric materials refer to the solid solution formed between Mg_2Si and Mg_2Sn, both of which have the same antifluorite crystal structure. The lattice thermal conductivity κ can be greatly reduced in such solid-solution phases compared with single Mg_2Si or Mg_2Sn phase through alloy scattering of heat-conducting phonons.[6–8] The bandgap of the solid-solution phase can be engineered by adjusting the Mg_2Si/Mg_2Sn ratio to achieve convergence of the light and heavy conduction bands, leading to a high Seebeck coefficient.[9,10] The electrical conductivity of undoped $Mg_2(Si,Sn)$-based materials is poor but can be improved by doping. The reported ZT values of $Mg_2(Si,Sn)$-based materials are generally in the range of 0.9 to 1.25,[8,11–13] in which Sb or Bi is commonly used as a dopant and the Mg/Si/Sn ratios are carefully adjusted to yield the maximum ZT.

Understanding the temperature-dependent mechanical properties of these $Mg_2(Si,Sn)$-based materials is as important as optimizing the ZT value, if the materials are to be made into practical devices; For example, the thermal gradient required for a thermoelectric material to function also imposes a stress, Λ, associated with the difference between the hot-side temperature, T_{hot}, and the cold-side temperature, T_{cold}, where Λ may be estimated as[14–16]

$$\Lambda = \frac{E(T)}{1-\mu(T)}\alpha(T)(T_{hot} - T_{cold}), \qquad (2)$$

where $E(T)$, $\mu(T)$, and $\alpha(T)$ are the temperature-dependent Young's modulus, Poisson's ratio, and linear coefficient of thermal expansion, respectively. Especially in waste heat recovery operations, the TE materials also experience thermal transients due to cold startups and hot shutdowns. The maximum surface stress, Λ_{max}, due to these transients can be approximated as[14–16]

$$\Lambda_{max} = \frac{E(T)}{1-\mu(T)}\alpha(T)\cdot(T_i - T_\infty)\cdot f(\mathrm{Bi}), \qquad (3)$$

where $(T_i - T_\infty)$ is the quench temperature difference and $f(\mathrm{Bi})$ is a function of the dimensionless Biot modulus, Bi. The Biot modulus is in turn defined as $\mathrm{Bi} = ah/\kappa$, where a is the characteristic specimen dimension, h is the surface heat transfer coefficient, and κ is the thermal conductivity.[14–16] In addition, in Eq. 2, if one replaces the thermal strain term, $\alpha(T)(T_{hot} - T_{cold})$ with the mechanical strain, then one can also express the stresses imposed by mechanical sources (such as vibration) in terms of E and μ.

In addition to the analytical expressions for stress, such as Eqs. 2 and 3, numerical stress calculations also require elasticity data; For example, E and μ are required to construct the stiffness matrix for finite-element computations of either thermally or mechanically imposed stresses.[17,18]

In addition to the elasticity, other mechanical properties such as the hardness and fracture toughness are also important, since hardness is an indication of the susceptibility of a material to damage by abrasion during processing or use[19] and toughness is a measure of a material's resistance to crack growth.[20] Although the mechanical properties are important to the design and implementation of thermoelectric devices, in general the literature data on thermoelectric materials are very limited and there are no data available on the elastic moduli, hardness or fracture toughness of $Mg_{2.08}Si_{0.4}Sn_{0.6}$.

In this research, we utilized two of the most time-efficient processing methods to make $Mg_2(Si,Sn)$-based materials, namely the flux-sealing synthesis method[12] and the pulsed electric current sintering (PECS) technique.[21] We were able to synthesize the materials with a yield of ~65 g/run. The nominal Si/Sn ratio was chosen to be 0.4/0.6 based on literature regarding the band-structure engineering of the compounds and the pseudobinary phase diagram of the Mg_2Si–Mg_2Sn system.[6,7] The optimal Mg content was determined through trial and error to be 2.08, which was used to compensate for the loss of Mg during synthesis. The Sb content was adjusted, and the Sb-concentration-dependent properties of the $Mg_{2.08}Si_{0.4-x}Sn_{0.6}Sb_x$ materials were then systematically investigated. The mechanical properties of the undoped $Mg_{2.08}Si_{0.4}Sn_{0.6}$ sample were evaluated from 295 K to 603 K.

EXPERIMENTAL PROCEDURES

Materials and Specimen Preparation

$Mg_{2.08}Si_{0.4-x}Sn_{0.6}Sb_x$ (x = 0, 0.012, 0.024, 0.036, 0.048, 0.060, and 0.072) compounds were synthesized using the B_2O_3 flux synthesis method in air in a box furnace.[12] Stoichiometric amounts of elemental Mg (99.8%), Si (99.9%), Sn (99.95%), and Sb (99.999%) powders were purchased from Alfa Aesar. The powders were weighed and homogeneously mixed in Al_2O_3 crucibles purchased from Almath Crucibles Ltd. Excess Mg was used to compensate for the loss of Mg during the succeeding synthesis and sintering process. The mixture was compacted and covered by a graphite foil. B_2O_3 powder was placed on top of the graphite foil and gently pressed before the alumina crucible was transferred from an argon-filled glovebox to a box furnace which was preheated to 700°C. The mixed powders were annealed at 700°C for 12 h in air. After the material had naturally cooled to room temperature, the alumina crucible was broken to separate the B_2O_3 seal from the cast ingot. The cast ingot was ground using an agate mortar and pestle in a glovebox flushed with flowing argon gas. The ground materials were passed through a 53-μm sieve. The sieved powders were densified using a PECS system at 30 MPa and

700°C for 15 min in a 304 stainless-steel die with inner diameter of 12.7 cm.

Specimen Characterization

The sample powders were characterized using a Rigaku MiniFlex x-ray diffractometer with a Cu K_α radiation source. Energy-dispersive x-ray (EDX) analysis was done on pieces cut from the densified pellets, using a JEOL 7500F field-emission scanning electron microscope (Oxford EDS). The density (ρ_0) of the pellets was measured by the Archimedes method using ethanol at room temperature. A Netzsch DIL 402 C dilatometer with a heating rate of 5 K/min was used to measure the linear coefficient of expansion of the sample from room temperature to 723 K, and the temperature-dependent density was calculated as

$$\rho_t = \rho_0/(1 + 3\alpha\Delta T). \quad (4)$$

Transport Property Measurements

The thermal diffusivity (D) of the samples was measured using a Netzsch LFA 457 system. The specific heat (C_p) was measured using the same system with stainless steel as a reference material. The thermal conductivity was then calculated as

$$\kappa = D \cdot \rho_t \cdot C_p. \quad (5)$$

The temperature-dependent electrical conductivity and Seebeck coefficient were measured using a ZEM-3 system (ULVAC Technologies, Inc.). The temperature-dependent carrier concentration and Hall mobility were measured using a laboratory-built Hall-effect apparatus[22] with a Hall-bar configuration.

Mechanical Property Measurements

The room-temperature hardness, H, and fracture toughness, K_C, were measured by Vickers indentation on undoped $Mg_{2.08}Si_{0.4}Sn_{0.6}$ samples. Polished specimens were indented 10 times each with 0.98 N, 1.96 N, 2.94 N, and 4.90 N loads using a microhardness tester (HMV-2000; Shimadzu, Kyoto, Japan) calibrated with a steel hardness standard (761-048; Yamamoto Scientific Tool Laboratory Co., Ltd., Japan). The hardness, H, was determined using the equation

$$H = \frac{1.854P}{(2a)^2}, \quad (6)$$

where P is the indenter load and $2a$ is the diagonal indentation length.[20] The fracture toughness, K_C, was determined from the radial crack length of the indentations, $2c$, using the equation

$$K_C = \frac{\xi(E/H)^{1/2}}{c^{3/2}}, \quad (7)$$

where E is the Young's modulus and ξ is a dimensionless constant assumed to be 0.016 based on previous study.[20]

The elastic moduli, longitudinal acoustic wave speed v_L, and shear acoustic wave speed v_S were determined over the range from room temperature to 603 K by resonant ultrasound spectroscopy (RUS) using commercial instrument (RUSpec; Magnaflux Quasar, Albuquerque, NM, USA).

The Debye temperature, θ_D, was calculated using the Anderson approximation[23]

$$\theta_D = \frac{h}{k_B}\left[\frac{3q}{4\pi}\frac{N_A\rho}{M}\right]^{1/3} V_m, \quad (8)$$

where h is Planck's constant, k_B is Boltzmann's constant, N_A is Avogadro's number, ρ is the mass density, M is the molecular weight, and q is the number of atoms per formula unit. The average acoustic velocity, v_M, was calculated from v_L and v_S as[23]

$$v_M = \left(\frac{1}{3}\left[\frac{2}{v_S^3} + \frac{1}{v_L^3}\right]\right)^{-1/3}. \quad (9)$$

High-temperature elastic moduli were measured by RUS using high-temperature transducers within a furnace with flowing Ar-4%H_2 gas. The furnace was heated to 303 K, then to 603 K in 30-K increments. At each temperature increment, the specimen was held at temperature for at least 5 min before the RUS measurement. Correction for the change in specimen dimensions as a function of temperature during high-temperature elasticity measurements was made using the coefficient of thermal expansion obtained from the Netzsch DIL 402 C dilatometer measurements mentioned above. Additional details of the RUS experimental procedure are provided elsewhere.[24–27]

RESULTS AND DISCUSSION

The densities of the samples were found to be 3.01 g/cm^3 to 3.24 g/cm^3, and the linear coefficient of expansion was measured to be $\alpha = 20 \times 10^{-6}$/K from room temperature to 723 K.

EDX Analysis

Two batches of samples were made, and the EDX results are presented in Table I. The carbon and oxygen signals were excluded from the raw EDX spectra. The samples for EDX analysis were randomly taken from pieces cut off from PECS-densified pellets.

Table I shows that the materials are Mg deficient, despite the excess Mg added to the starting material. The Si content was also less than the nominal content, while the Sn and Sb contents exceeded the starting composition. This could be due to material loss through sublimation, or from nonuniformities

Table I. EDX-characterized composition of $Mg_{2.08}Si_{0.4-x}Sn_{0.6}Sb_x$ samples

1st batch	x = 0.000	x = 0.012	x = 0.024	x = 0.036
Mg	1.86	1.84	1.66	1.80
Si	0.37	0.38	0.38	0.33
Sn	0.63	0.58	0.58	0.62
Sb	0	0.038	0.040	0.053

2nd batch	x = 0.000	x = 0.012	x = 0.024	x = 0.036	x = 0.048	x = 0.060	x = 0.072
Mg	1.74	1.78	1.61	1.76	1.71	1.82	1.81
Si	0.37	0.36	0.30	0.30	0.31	0.26	0.31
Sn	0.63	0.64	0.67	0.66	0.65	0.69	0.60
Sb	0	0	0.041	0.044	0.047	0.058	0.085

in the resulting ingot since the interface between the B_2O_3 and the $Mg_{2.08}Si_{0.4-x}Sn_{0.6}Sb_x$ compound was removed prior to powder processing.

The results presented in the rest of this paper are from the second batch of samples (Table I), with the data labeled according to the nominal compositions. The effect of the Mg loss is discussed at the end of the transport property discussion.

Powder x-Ray Diffraction Spectra

The as-synthesized ingots were ground and scanned in the x-ray diffractometer before being sintered by PECS. The densified pellets were ground into powder form after the transport property measurements and scanned in the x-ray diffractometer again. The x-ray diffraction spectra of the powders before and after PECS processing are shown in Fig. 1.

All the x-ray diffraction spectra indicate the formation of the Mg_2Si–Mg_2Sn solid-solution phases compared with the standard diffraction spectra of Mg_2Si and Mg_2Sn. In some of the as-synthesized samples, diffraction peaks from unreacted Mg were found, but such impurity peaks were eliminated after the PECS process. For some of the as-synthesized powders, characteristic peaks were accompanied by a close secondary peak shoulder, possibly indicating incomplete mixing of the Mg_2Si and Mg_2Sn phases. After grinding and PECS processing, no secondary peaks were observed and a single solid-solution phase was obtained.

Transport Properties

The temperature-dependent electrical conductivity, Seebeck coefficient, power factor, thermal conductivity, and ZT value of the $Mg_{2.08}Si_{0.4-x}Sn_{0.6}Sb_x$ (x = 0, 0.012, 0.024, 0.036, 0.048, 0.060, and 0.072) compounds are shown in Figs. 2, 3, 4, 5a, and 6, respectively. The specific heat values measured using the LFA 457 are also shown in Fig. 5b. The two horizontal dashed lines in Fig. 5b represent the theoretical values of C_v calculated based on the Dulong–Petit law[28] using the following equation:

$$C_vM = 3R, \tag{10}$$

where M is the averaged molar mass and R is the gas constant. The upper and lower lines were calculated using the averaged molar mass of the x = 0 and x = 0.060 samples, respectively (Fig. 5b).

All compounds exhibited negative Seebeck coefficients, showing intrinsic n-type behavior and indicating that Sb acts as an electron donor in this system, in agreement with previous reports.[8,9,29] The electrical conductivity of the compounds increased with increasing Sb concentration for $0 \le x \le 0.048$, while the magnitude of the Seebeck coefficient decreased with increasing Sb concentration, as shown in Figs. 2 and 3. The Sb doping saturated for $x \ge 0.060$, and the carrier concentration

started to decrease when the doping level was increased further. As a result, the electrical conductivity of the two most heavily doped samples (x = 0.060 and x = 0.072) was lower than that of the sample with x = 0.048, while the absolute Seebeck coefficients were greater than that of the sample with x = 0.048.

The magnitude of the Seebeck coefficient for the x = 0 sample peaked at approximately 460 K and dropped at elevated temperatures (460 K to 760 K). This effect can be explained by bipolar conduction at elevated temperatures when the minority carriers start opposing the Seebeck effect of the majority carriers. For the lightly doped samples (x = 0.012 and 0.024), this bipolar effect is still observable in the high-temperature range. The thermal conductivity of the samples generally decreased as the temperature was increased from room temperature, due to the stronger lattice vibrations at elevated temperatures. Bipolar contributions to the thermal conductivity can also be seen in thermal conductivity at high temperatures as shown below.

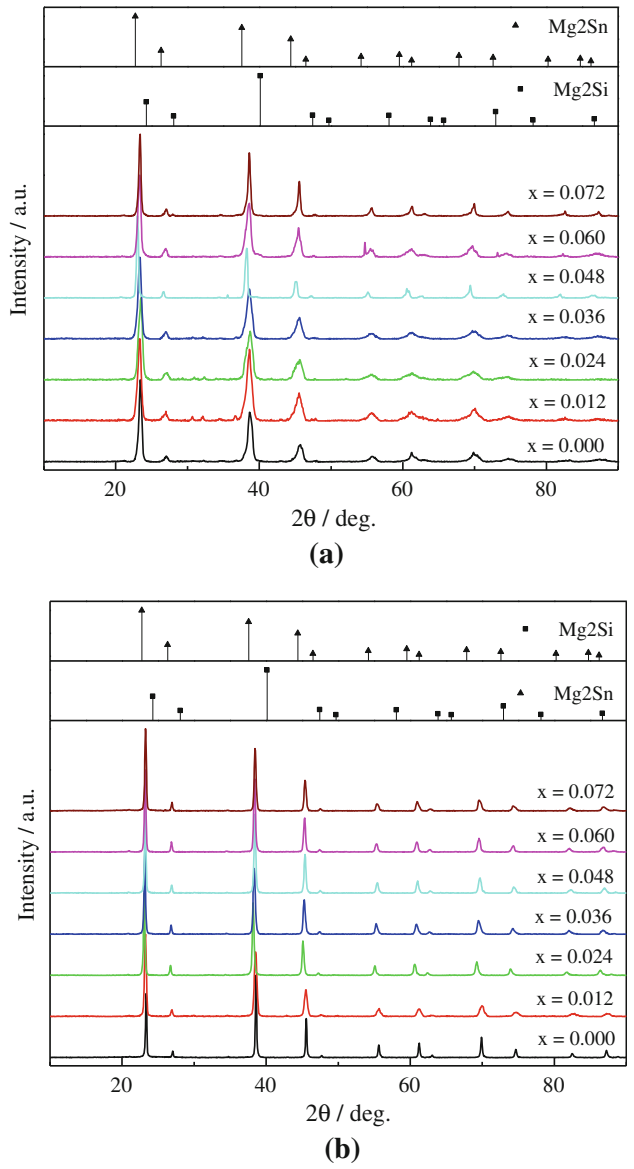

Fig. 1. XRD patterns (a) before and (b) after PECS, showing some sharpening of the peaks after PECS processing.

Carrier Concentration and Hall Mobility

The undoped sample (x = 0) showed typical intrinsic behavior, which was used to estimate the bandgap, E_g, of the materials by fitting the temperature-dependent carrier concentration n to the following equation:

$$n = 2 \times \left(\frac{2\pi m^* k_B T}{h^2}\right)^{3/2} \exp\left(-\frac{E_g}{2k_B T}\right), \qquad (11)$$

where m^* is the effective mass, k_B is the Boltzmann constant, T is temperature in Kelvin, h is the Planck constant, E_C is the energy level of the bottom of the conduction band, and E_F is the Fermi level. The assumption that the Fermi level of an intrinsic semiconductor lies at the middle of the bandgap was used, and the temperature dependence of the bandgap was neglected. A bandgap of E_g = 0.594 eV was obtained in this way, which is in very good agreement with that estimated by Isachenko et al.[30]

A maximum ZT value of 1.50 at 716 K was found for the $Mg_{2.08}Si_{0.364}Sn_{0.6}Sb_{0.036}$ sample. $ZT > 1$ was repeatedly obtained in the moderately and heavily doped samples ($x \geq 0.024$). Assuming that the bandgap does not change with varying dopant concentration or with temperature, then

$$\frac{E_g}{k_B T} \approx 9.62$$

at 716 K for the $Mg_{2.08}Si_{0.364}Sn_{0.6}Sb_{0.036}$ sample, which agrees well with the $10k_BT$ guideline pro-

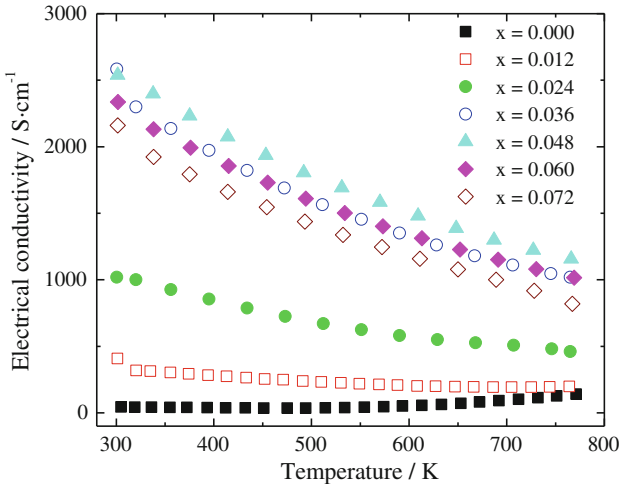

Fig. 2. Electrical conductivity versus temperature for nominal compositions $Mg_{2.08}Si_{0.4-x}Sn_{0.6}Sb_x$.

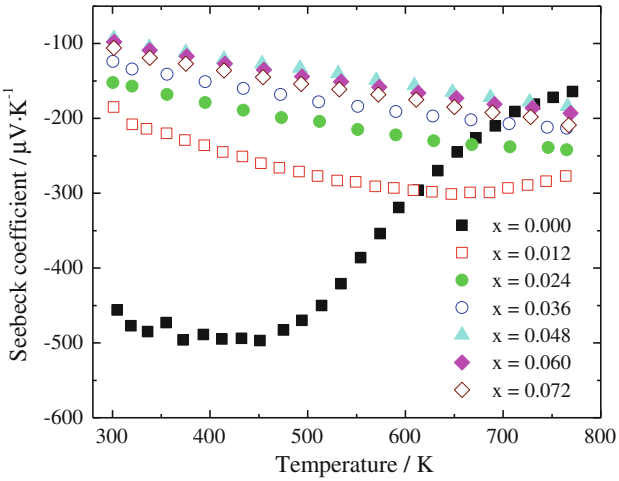

Fig. 3. Seebeck coefficient versus temperature for nominal compositions $Mg_{2.08}Si_{0.4-x}Sn_{0.6}Sb_x$.

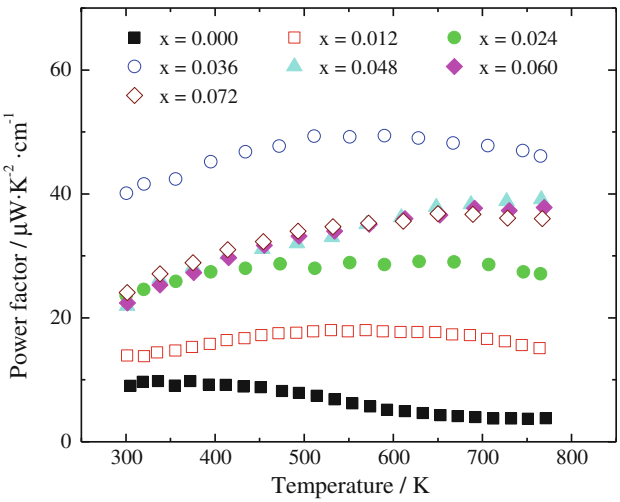

Fig. 4. Power factor versus temperature for nominal compositions $Mg_{2.08}Si_{0.4-x}Sn_{0.6}Sb_x$.

posed by Mahan[31] and helps explain the large ZT value for this compound in terms of bandgap engineering (Figs. 7 and 8).[29,32,33]

The Hall mobility is shown in Fig. 9 on a logarithmic scale. Only the results for undoped and moderately doped samples ($x \leq 0.036$) are shown due to measurement system limitations for the heavily doped samples. The temperature dependence of the Hall mobility generally follows the relation

$$\mu_H \propto T^j,$$

where $j = -0.5$ corresponds to alloy scattering and $j = -1.5$ indicates acoustic phonon scattering. For most of the Hall mobility data, j falls in the range between -1.5 and -0.5, indicating a mixed scattering mechanism. We were able to fit the measured Hall mobility to the empirical equation[34]

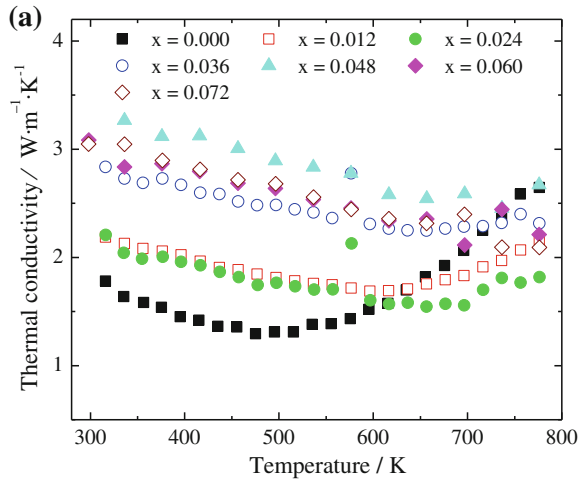

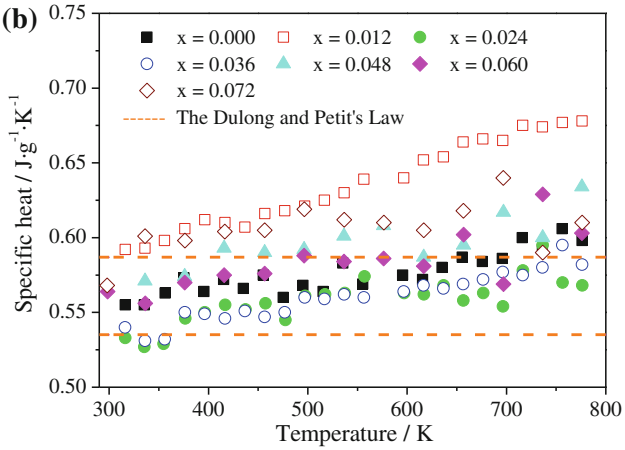

Fig. 5. (a) Thermal conductivity and (b) specific heat versus temperature for nominal compositions $Mg_{2.08}Si_{0.4-x}Sn_{0.6}Sb_x$.

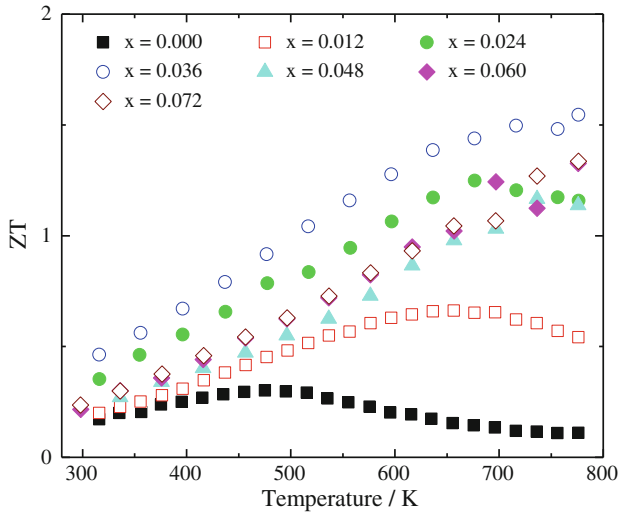

Fig. 6. Figure of merit ZT versus temperature for nominal compositions $Mg_{2.08}Si_{0.4-x}Sn_{0.6}Sb_x$.

$$\frac{1}{\mu_H} = \frac{1}{\mu_{al}}\left(\frac{T}{300\,K}\right)^{0.5} + \frac{1}{\mu_{ph}}\left(\frac{T}{300\,K}\right)^{1.5}, \qquad (12)$$

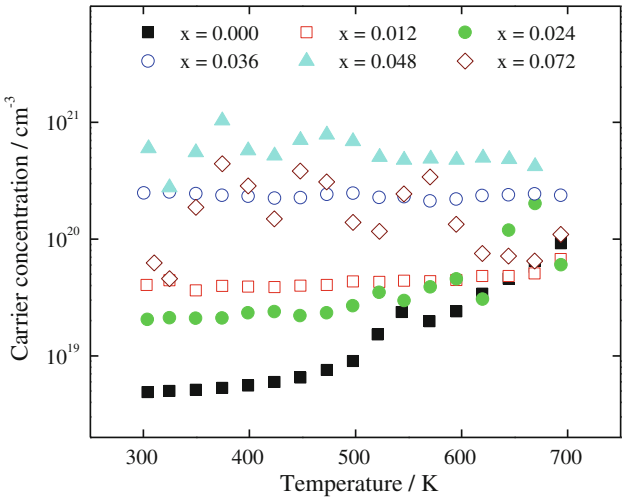

Fig. 7. Carrier concentration versus temperature for nominal compositions $Mg_{2.08}Si_{0.4-x}Sn_{0.6}Sb_x$.

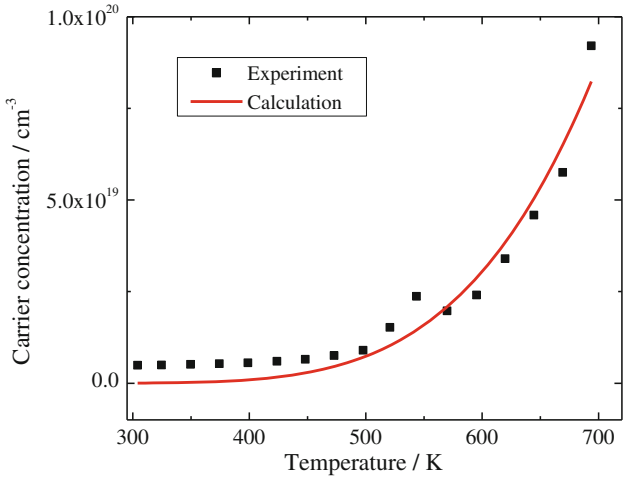

Fig. 8. Measured and calculated carrier concentration for $Mg_{2.08}Si_{0.4}Sn_{0.6}$.

where μ_{al} and μ_{ph} are the alloy disorder scattering mobility and acoustic phonon scattering mobility at room temperature, respectively. The fitting results are listed in Table II. The alloy scattering can be attributed to the formation of the Mg_2Si–Mg_2Sn solid solution as well as disorder induced by Mg vacancies. In addition, the value of μ_{al} decreases as the doping level increases, possibly indicating filling of the Mg vacancies. The values of μ_{ph} for the Sb-doped samples are higher than for the undoped sample, except for the $x = 0.024$ specimen. This result is in agreement with the effect of Mg vacancies in Mg-deficient $Mg_2Si_{1-x}Sb_x$ materials reported by Dasgupta et al.[35] We suspect that the small μ_{ph} value for $x = 0.024$ was caused by internal cracks, which could also explain the lower electrical conductivity measured using the ZEM-3 system and the Hall measurement system.

Analysis Using a Single Parabolic Band Model

A single parabolic band model was employed to quantitatively analyze the temperature-dependent transport behavior of the compounds, in which the Seebeck coefficient S of the material was expressed as

$$S = -\frac{k_B}{e}\left[\frac{(\frac{5}{2}+\lambda)F_{3/2+\lambda}}{(\frac{3}{2}+\lambda)F_{1/2+\lambda}} - \eta\right]$$
$$F_r = \int_0^\infty x^r f(\eta)\mathrm{d}x \qquad (13)$$
$$f(\eta) = \frac{1}{1+e^{x-\eta}}$$
$$\eta = \frac{E_C - E_F}{k_B T},$$

where λ is the scattering parameter, which was assumed to be $-1/2$ to describe a phonon scattering dominant mechanism. The reduced chemical potential was found from the measured Seebeck coefficient, and the effective mass was determined from the measured carrier concentration using

$$n = \frac{4}{\sqrt{\pi}}\left(\frac{2\pi m^* k_B T}{h^2}\right)^{3/2} F_{1/2}(\eta). \qquad (14)$$

Figure 10 shows the relationship between the effective mass and carrier concentration for the doped samples at room temperature. The effective mass ranges between $1.1m_0$ and $3.33m_0$, where m_0 is the free electron mass, which are comparable to the values reported by Du et al.[36] and Zaitsev et al.[9] The carrier concentration increases as the effective mass increases. A similar effective mass dependence on Sb doping was reported for $Mg_2Si_{1-x}Sb_x$ materials by Dasgupta et al.,[35] but there has been no theoretical support for a similar effect in $Mg_2Si_{0.4-x}Sn_{0.6}Sb_x$ materials. Further study is needed to reveal the doping mechanism of Sb and the role of Mg vacancies in Mg_2Si–Mg_2Sn solid solutions.

The lattice (κ_L), electronic (κ_e), and bipolar (κ_{bp}) components of the thermal conductivity of the compounds can be extracted by using the following relations:

$$\kappa = \kappa_e + \kappa_L + \kappa_{bp}, \qquad (15)$$

where κ_e can be calculated using the Wiedemann–Franz law,[37]

$$\kappa_e = L_0 \sigma T, \qquad (16)$$

$$L_0 = \left(\frac{k_B}{e}\right)^2 \left[\frac{(\lambda+7/2)F_{\lambda+5/2}(\eta)}{(\lambda+3/2)F_{\lambda+1/2}(\eta)} - \delta^2(\eta)\right], \qquad (17)$$

$$\delta(\eta) = \frac{(\lambda+5/2)F_{\lambda+3/2}(\eta)}{(\lambda+3/2)F_{\lambda+1/2}(\eta)}.$$

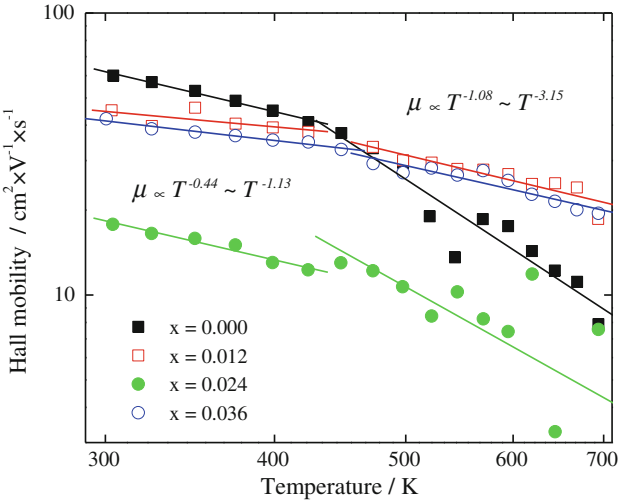

Fig. 9. Hall mobility for $Mg_{2.08}Si_{0.4-x}Sn_{0.6}Sb_x$.

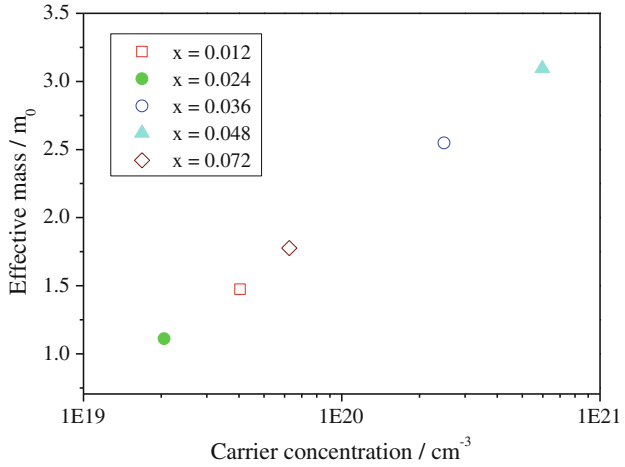

Fig. 10. Effective mass versus carrier concentration.

Table II. Results of fitting the Hall mobility using the empirical Eq. 12

	$x = 0.000$	$x = 0.012$	$x = 0.024$	$x = 0.036$
μ_{al} (cm^2/V-s)	1750.55	65.16	68.37	52.52
μ_{ph} (cm^2/V-s)	62.51	171.88	26.08	206.59

The calculated Lorenz numbers, L_0, fall between 1.5×10^{-8} V^2/K^2 and 2.0×10^{-8} V^2/K^2, typical for semiconductors.

The thermal conductivity components $\kappa_L + \kappa_{bp}$ are plotted against $1/T$ in Fig. 11. A two conduction band model could be helpful in extracting the κ_{bp} component from the total thermal conductivity, for which suitable electron–hole effective mass and mobility ratios are needed. Because bipolar conduction only becomes appreciable at elevated temperatures, in the relatively low temperature range, $\kappa_L + \kappa_{bp}$ could be treated approximately as κ_L. Thus, we were able to use the Keyes relation[38] to fit the experimental data in selected temperature ranges where the bipolar contribution is small. The Keyes relation is stated as

$$\kappa T = \left[\frac{R^{3/2}T_m^{3/2}}{3\gamma^2\varepsilon^3 N_0^{1/3}}\right]\frac{\rho^{2/3}}{A^{7/6}}, \qquad (18)$$

where R is the universal gas constant, γ is the Grüneisen parameter, ε is the ratio of the atomic vibrations to the lattice constant during melting of a solid, N_0 is Avogadro's number, T_m is the melting point of the material, ρ is the density, and A is the average atomic weight. The slope of Eq. 18 obtained from the least-squares fit gives the value of the term on the right-hand side of Eq. 18, in which A and ρ could be directly measured. Then the bracketed term in Eq. 18 was calculated as shown in Table III.

Comparing the lattice thermal conductivity of samples with different doping levels shows that the lowest lattice thermal conductivity was found in the sample with the smallest bracketed term. A lower numerical magnitude of the bracketed term in Eq. 16 could be caused by a melting point change or a change of the Grüneisen parameter, both of which depend on the Sb doping.

Mg Vacancies and Sb Filling Effects

The effect of Mg vacancies and Sb filling was found both experimentally[35] and theoretically[39] in work done on $Mg_2Si_{1-x}Sb_x$ compounds, as the Mg vacancies act as double-hole donors and compensate for the extra electrons introduced by Sb. Compared with other reported work on this material system,[11,13] more Sb was needed in this research to obtain the same carrier concentration (Table IV). Considering the EDX results presented in Table I, which show Mg deficiency in all the samples, similar effects of Mg vacancy formation and Sb filling might be possible in $Mg_2Si_{04-x}Sn_{0.6}Sb_x$ compounds as well. A more detailed and accurate analysis on the chemical and phase composition along with further theoretical work is necessary to help understand those results.

Comparison with Other Reports of High ZT

High ZT values of 1.43 ($x = 0.036$, denoted as PG1 in the following discussion) and 1.50 ($x = 0.036$ repeat, denoted as PG2 in the following discussion) in this work were obtained for samples with the same nominal composition. To better understand the reason for these high ZT values, a detailed comparison of the electrical conductivity, Seebeck coefficient, and thermal conductivity for the samples with the highest ZT values reported by different groups is shown in Figs. 12–16.

The high *ZT* values measured in this work can be attributed to high electrical conductivity and reduced thermal conductivity.

The PG2 sample (Fig. 13) had comparable Seebeck coefficient to all other works, which indicates that the carrier concentrations of all the samples with high *ZT* reported by different groups are comparable (Table IV). The PG2 sample exhibits much higher electrical conductivity than the other works, except for Zaitsev's work where the increase is less than 10%. As shown in Table IV, Zaitsev's sample had the closest chemical composition ($Mg_2Si_{0.4}Sn_{0.6}$) to the composition in this work, while the work of the other three researchers was based on $Mg_2Si_{0.5}Sn_{0.5}$ or $Mg_2Si_{0.6}Sn_{0.4}$ solid solutions. Søndergaard showed that $Mg_2Si_{0.4}Sn_{0.6}$ solid solutions had higher electrical transport properties than $Mg_2Si_{0.5}Sn_{0.5}$ or $Mg_2Si_{0.6}Sn_{0.4}$ solid solutions when doped to the same level.[13] Considering the comparable Seebeck coefficients, the high electrical conductivities of the PG2 sample and Zaitsev's sample should be attributed to the high mobilities of these samples. The thermal conductivity of the PG2 sample is comparable to the values reported by Gao et al.,[12] Liu et al.,[11] and Søndergaard et al.[13]

The PG1 sample had lower electrical conductivity, higher absolute Seebeck coefficient, and lower thermal conductivity than all other samples including the PG2 sample. The results for samples PG1 and PG2 are consistent with the changes of electrical conductivity and Seebeck coefficient following Mott's equation,[40] and the reduced thermal conductivity of PG1 can be attributed to the reduced electrical contribution to the thermal conductivity.

The lattice and bipolar (nonelectrical) thermal conductivity of the PG2 sample was lower than Gao's and Liu's results. The reason for this is not clear, but similar results were found in Dasgupta's work[35] in which the Mg vacancies could possibly reduce the lattice thermal conductivity of the $Mg_2Si_{1-x}Sb_x$ compounds.

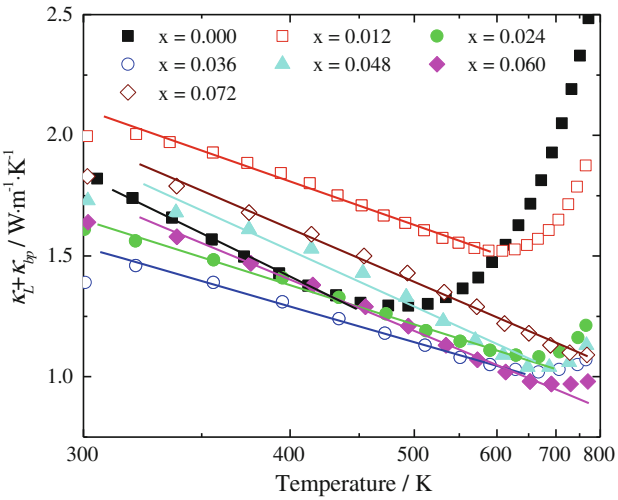

Fig. 11. Lattice and bipolar thermal conductivity ($\kappa_L + \kappa_{bp}$).

MECHANICAL PROPERTIES

Room-Temperature Measurements

As determined by RUS measurements, the room-temperature Young's modulus *E*, shear modulus *G*, and Poisson's ratio of $Mg_{2.08}Si_{0.4}Sn_{0.6}$ were 88.13 ± 0.15 GPa, 36.87 ± 0.04 GPa, and 0.195 ± 0.001, respectively. While the elastic moduli for the com-

Table III. Fitting results of Eq. 18 to the thermal conductivity from $\kappa_L + \kappa_{bp}$

	x = 0.000	*x* = 0.012	*x* = 0.024	*x* = 0.036	*x* = 0.048	*x* = 0.060	*x* = 0.072
Slope (a.u.)	501.3	359.9	324.4	295.2	465.0	425.0	440.5
ρ (g/cm)	3.01	3.01	3.24	3.06	3.02	3.08	3.06
A (g/mol)	46.52	46.62	50.462	48.862	48.94	49.61	47.92
Bracketed term (a.u)	21,224	18,282	14,369	13,091	20,830	19,086	19,086

Table IV. Comparison of optimal nominal Sb content from different literature reports

	ZT	Carrier Concentration (cm^{-3})	Composition
This work	1.51	2.35×10^{20}	$Mg_{2.08}Si_{0.364}Sn_{0.6}Sb_{0.036}$
Zaitsev[9]	1.0	2.99×10^{20}	$Mg_2Si_{0.4}Sn_{0.6}$ with Sb doping
Liu[11]	1.25	1.92×10^{20}	$Mg_{2.11}Si_{0.52}Sn_{0.48}Sb_{0.0056}$
Gao[12]	0.9	2.6×10^{20}	$Mg_{2+z}Si_{0.487}Sn_{0.5}Sb_{0.013}$*
Søndergaard[13]	1.0	1.6×10^{20}	$Mg_{2.2}Si_{0.5925}Sn_{0.4}Sb_{0.0075}$

* The exact composition (*z* value) was not specified in Gao's original paper.

position $Mg_{2.08}Si_{0.4}Sn_{0.6}$ are not available in the literature, Table V lists elasticity data for several literature studies of Mg_2Si including two experimental studies,[41,42] elasticity calculations based on density functional theory,[43] and a room-temperature polycrystalline average of single-crystal data.[44] The E values of Mg_2Si are about 20% higher than the E value of 88.13 ± 0.15 GPa found for $Mg_{2.08}Si_{0.4}Sn_{0.6}$ in this study. However, Mg_2Si and Mg_2Sn can be considered as end-members for the solid solution $Mg_{2.08}Si_{0.4}Sn_{0.6}$, where E for Mg_2Sn has been reported as 80.3 GPa, and thus the E value for $Mg_{2.08}Si_{0.4}Sn_{0.6}$ is intermediate to the E values for Mg_2Si and Mg_2Sn. Also, as discussed by Ren et al.,[45] the elastic moduli of solid solutions can vary as a function of composition by up to 20% or 30% from the Young's moduli of the end-members. In addition, the Poisson's ratio measured in this study for $Mg_{2.08}Si_{0.4}Sn_{0.6}$ (0.195 ± 0.001) coincides with the upper range of literature values for Mg_2Si and Mg_2Sn (Table V).

For $Mg_{2.08}Si_{0.4}Sn_{0.6}$, the mean ± standard deviation of the Vickers indentation hardness, H, was

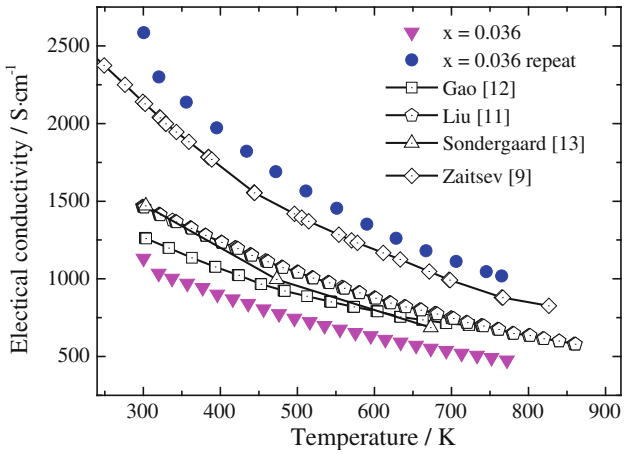

Fig. 12. Comparison of electrical conductivity from different groups.

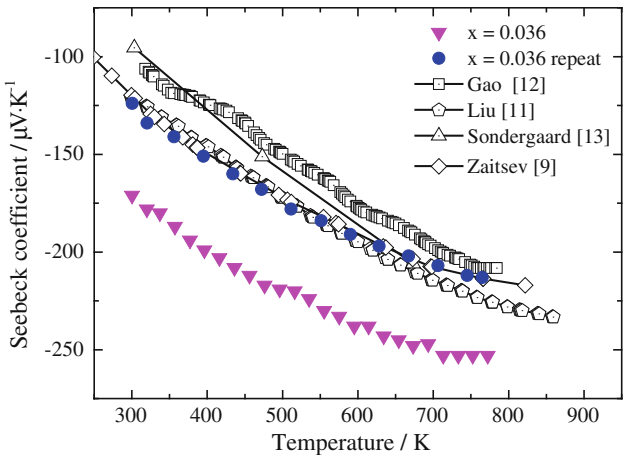

Fig. 13. Comparison of Seebeck coefficient from different groups.

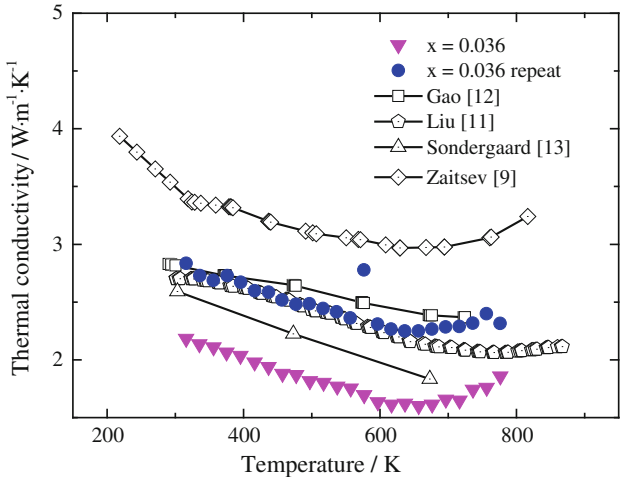

Fig. 14. Comparison of thermal conductivity from different groups.

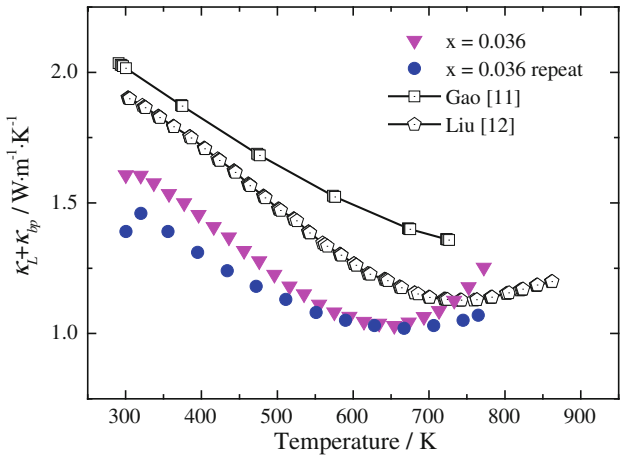

Fig. 15. Comparison of lattice and bipolar thermal conductivity (κ_L + κ_{bp}) from different groups.

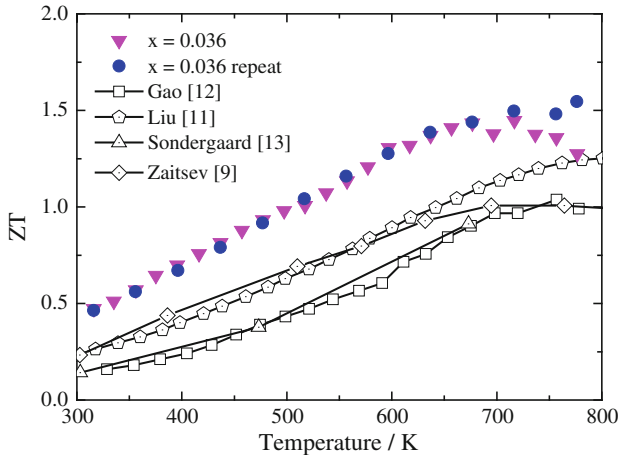

Fig. 16. Comparison of ZT values from different groups.

Table V. Literature data for the room-temperature Young's modulus E, shear modulus G, Poisson's ratio μ, hardness H, and fracture toughness K_C for Mg_2Si- and Mg_2Sn-based thermoelectric materials

Composition	E (GPa)	G (GPa)	μ	H (GPa)	K_C (MPa m$^{1/2}$)	Density (g/cm^3)	Reference
Mg_2Sn	80.3[a]	34.2[a]	0.176[a]	NA	NA	3.592	56
Mg_2Sn	NA	NA	NA	1.17	NA	NA	47
Mg_2Si	117.3	49.5	0.175–0.195	5.3	1.3	2.07	42
Mg_2Si	114.32[b]	48.82[b]	0.171[b]	NA	NA	NA	43
Mg_2Si	110.9[a]	47.6[a]	0.164[a]	NA	NA	NA	44
Mg_2Si	76 ± 6[c]	NA	NA	3.96–4.20	0.81–0.97	1.94	41
Mg_2Si	NA	NA	NA	4.38	NA	1.99	46

NA not available[a]Calculated from first principles based on density functional theory[43][b]Calculated from the room-temperature polycrystalline average of single-crystal data[44][c]Recognized by authors in Ref. 41 as a lower E than typically reported for Mg_2Si.

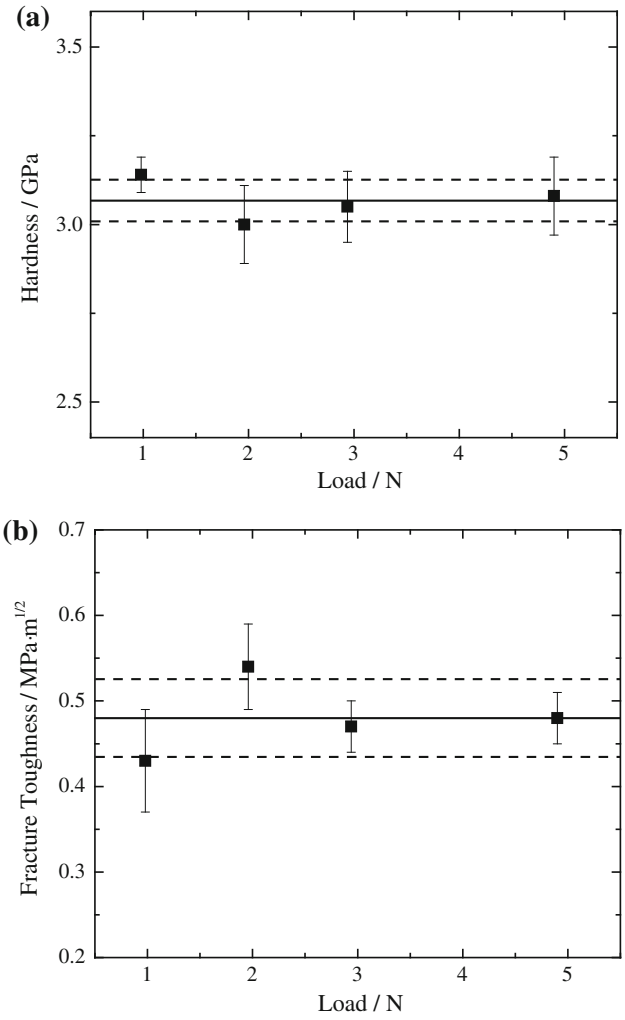

Fig. 17. (a) Hardness versus load and (b) fracture toughness versus load. The solid horizontal line indicates (a) the mean hardness and (b) the mean K_C over the load range, while the dashed lines represent the standard deviation.

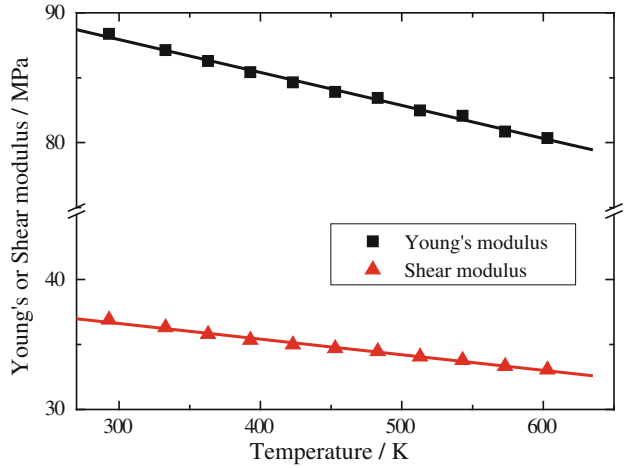

Fig. 18. Young's and shear moduli as a function of temperature.

3.07 ± 0.06 GPa for the load range between 0.98 N and 4.90 N (Fig. 17a). As is the case for the elasticity data, no H data exist in the literature for $Mg_{2.08}Si_{0.4}Sn_{0.6}$. However, the literature values of H for Mg_2Si and Mg_2Sn (Table V) bracket the H value found in this study for $Mg_{2.08}Si_{0.4}Sn_{0.6}$, with H for Mg_2Si ranging from 3.96 GPa to 5.3 GPa[41,42,46] and an H value for Mg_2Sn of 1.17 GPa.[47] In comparison with other thermoelectric materials, the H values for $Mg_{2.08}Si_{0.4}Sn_{0.6}$ are intermediate between the Vickers hardness of chalcogenide-based thermoelectric materials [such as PbTe-8%PbS[25] and lead-antimony-silver-tellurium (LAST),[48] for which H ranges from about 0.5 GPa to 1.3 GPa] and some skutterudite materials with H values exceeding 5 GPa.[49]

The mean fracture toughness, K_C, was 0.48 ± 0.05 MPa m$^{1/2}$ for $Mg_{2.08}Si_{0.4}Sn_{0.6}$ (Fig. 17b), being essentially independent of load over the range from 0.98 N to 4.90 N. There are no K_C data in the literature for Mg_2Sn or $Mg_{2.08}Si_{0.4}Sn_{0.6}$, but a value of 1.3 MPa m$^{1/2}$ has been reported for Mg_2Si. Comparing more broadly with other thermoelectric materials, the K_C value for $Mg_{2.08}Si_{0.4}Sn_{0.6}$ from this study is essentially the same as the value of 0.47 ± 0.05 MPa m$^{1/2}$ recently reported for natural mineral tetrahedrite ($Cu_{10}Zn_2As_4S_{13}$)-based thermoelectrics.[50] In addition, for both of the chalcogenides PbTe-8%PbS[25] and LAST,[51] K_C is about 0.35 MPa m$^{1/2}$, while for the low-temperature

intermetallic thermoelectric $YbAl_3$, K_C values of up to 1.7 MPa $m^{1/2}$ have been reported.[52]

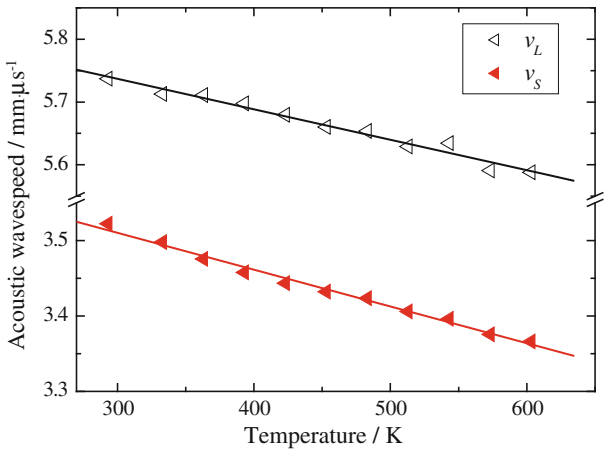

Fig. 19. Longitudinal and shear acoustic velocities, v_L and v_S, as a function of temperature.

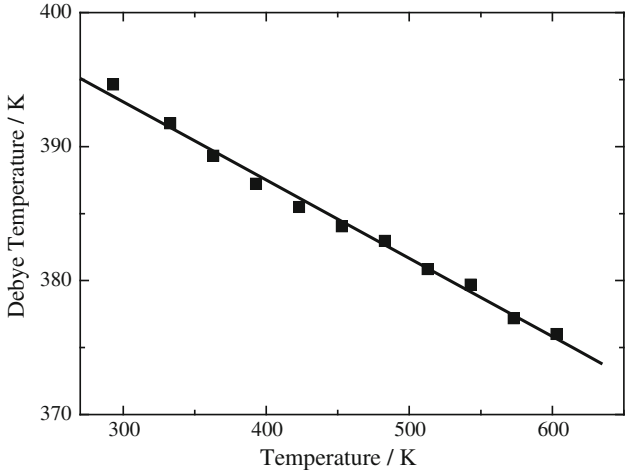

Fig. 20. Debye temperature as a function of temperature.

Temperature-Dependent Elastic Measurements

The temperature-dependent data for E and G (Fig. 18), as well as the longitudinal and shear acoustic velocities, v_L and v_S (Fig. 19), and the Debye temperature θ_D (Fig. 20), were least-squares fit using the linear equation

$$A = A_{RT}(1 - b_A[T - T_{RT}]), \quad (19)$$

where A is E, G, v_L, v_S or θ_D, A_{RT} is the room-temperature intercept of property A, T is measurement temperature, T_{RT} is room temperature, and b_A is the slope of A versus T. Table VI lists the resulting fitting parameters A_{RT} and b_A. Equation 19 describes the temperature-dependent changes of E, G, v_L, v_S or θ_D relatively well (Figs. 18–20).

For polycrystalline solids, including polycrystalline thermoelectric materials, the Young's and shear moduli typically decrease linearly with increasing temperature for temperatures greater than roughly $\theta_D/3$ to $\theta_D/5$.[27,51,53,54] As determined in this study, the acoustic Debye temperature for $Mg_{2.08}Si_{0.4}Sn_{0.6}$ ranged between approximately 394 K and 385 K for the interval from room temperature to 603 K (Fig. 20). Since the lower limit of measurement temperature in this study was room temperature, which in turn is much greater than $\theta_D/3$, the observed linear trend in E and G versus T agrees with what is expected based on the literature.[27,51,53,54] In addition, the linear dependence of the acoustic velocities v_L and v_S is consistent with the literature.[55]

The temperature-dependent Poisson's ratio data were not a linear function of temperature (Fig. 21). A least-squares fit of the temperature-dependent Poisson's ratio data to the empirical relationship for Poisson's ratio,

$$\mu = \mu_{RT} + c(T - T_{RT}) + d(T - T_{RT})^2 \quad (20)$$

yielded the following results: $\mu_{RT} = 0.1976 \pm 0.0005$, $c = (107.5 \pm 7.3) \times 10^{-6}$/K, and $d = (-17.55 \pm 0.02) \times 10^{-6}/K^2$ with a coefficient of determination, R^2, of 0.931.

Table VI. Fitting parameters A_{RT} and b_A for the least-squares fit of Young's modulus E, shear modulus G, the longitudinal and shear acoustic velocities v_L and v_S, and the Debye temperature θ_D in Eq. 19

Property	A_{RT}	b_A (10^{-4}/K)	R^2
E	88.07 ± 0.11 GPa	2.86 ± 0.06	0.995
G	36.63 ± 0.07 GPa	3.20 ± 0.10	0.991
v_L	5.740 ± 0.005 mm/μs	0.85 ± 0.04	0.975
v_S	3.513 ± 0.003 mm/μs	1.39 ± 0.05	0.990
θ_D	394 ± 0.3 K	1.48 ± 0.04	0.993

R^2 is the coefficient of determination in each case.

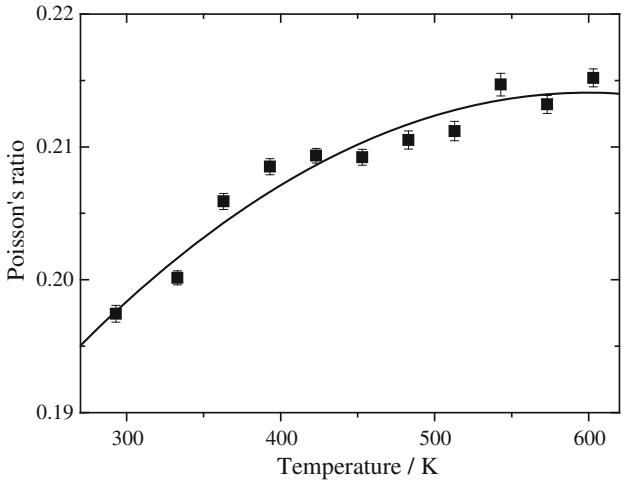

Fig. 21. Poisson's ratio as a function of temperature.

CONCLUSIONS

We combined two cost-effective processing techniques, i.e., flux synthesis and PECS, to make $Mg_{2.08}Si_{0.4-x}Sn_{0.6}Sb_x$ materials with yields of 16 g/run to 65 g/run. A maximum ZT of 1.50 at 716 K was found for $Mg_{2.08}Si_{0.364}Sn_{0.6}Sb_{0.036}$. $ZT > 1$ was repeatedly obtained in the moderately and heavily doped samples ($x \geq 0.024$). Further research is being conducted to further ascertain the influence of Mg deficiency in these compounds. This study includes the first measurements of the mechanical properties of $Mg_{2.08}Si_{0.4}Sn_{0.6}$. The measurements of the temperature-dependent Young's modulus and Poisson's ratio provide data needed to construct the stiffness matrix for finite-element analysis of stress and strain, which is in turn critical for the design of thermoelectric generators. In addition, the fracture toughness measurements are needed to predict the stress conditions for the onset of crack growth.

ACKNOWLEDGEMENTS

The authors acknowledge the financial support of the Department of Energy, "Revolutionary Materials for Solid State Energy Conversion Center," an Energy Frontiers Research Center funded by the US Department of Energy, Office of Science, Office of Basic Energy Sciences under Award Number DE-SC0001054. The authors also wish to acknowledge the gracious help from Karl Dersch in operating the PECS equipment.

REFERENCES

1. D.M. Rowe, *CRC Handbook of Thermoelectrics* (Boca Raton, FL: CRC Press, 1995).
2. J. Yang, *ICT 2005 24th International Conference on Thermoelectrics*, (2005), p. 170.
3. B.C. Blanke, J.H. Birden, K.C. Jordan, and E.L. Murphy, Report No. MLM-11271960.
4. R.J. Mehta, Y. Zhang, C. Karthik, B. Singh, R.W. Siegel, T. Borca-Tasciuc, and G. Ramanath, *Nat. Mater.* 11, 233 (2012).
5. K. Biswas, J. He, I.D. Blum, C.-I. Wu, T.P. Hogan, D.N. Seidman, V.P. Dravid, and M.G. Kanatzidis, *Nature* 489, 414 (2012).
6. V. Zaitsev, E. Tkalenko, and E. Nikitin, *Fiz Tverd Tela* 11, 3584 (1969).
7. T.J. Zhu, Y.Q. Cao, Q. Zhang, and X.B. Zhao, *J. Electron. Mater.* 39, 1990 (2009).
8. Y. Isoda, T. Nagai, H. Fujiu, Y. Imai, and Y. Shinohara, *ICT '06. 25th International Conference on Thermoelectrics* (2006), p. 406.
9. V.K. Zaitsev, M.I. Fedorov, E.A. Gurieva, I.S. Eremin, P.P. Konstantinov, A.Y. Samunin, and M.V. Vedernikov, *Phys. Rev. B* 74, 045207 (2006).
10. W. Liu, X. Tan, K. Yin, H. Liu, X. Tang, J. Shi, Q. Zhang, and C. Uher, *Phys. Rev. Lett.* 108, 166601 (2012).
11. W. Liu, X. Tang, H. Li, J. Sharp, X. Zhou, and C. Uher, *Chem. Mater.* 23, 5256 (2011).
12. H.L. Gao, T.J. Zhu, X.X. Liu, L.X. Chen, and X.B. Zhao, *J. Mater. Chem.* 21, 5933 (2011).
13. M. Søndergaard, M. Christensen, K.A. Borup, H. Yin, and B.B. Iversen, *J. Electron. Mater.* 42, 1417 (2013).
14. S.S. Manson, *Thermal Stress and Low-Cycle Fatigue* (New York: McGraw-Hill, 1966).
15. E.D. Case, *Thermomechanical Fatigue and Fracture*, ed. M.H. Alibadi (Southampton: WIT, 2002), .
16. L.G. Zhao, T.J. Lu, and N.A. Fleck, *J. Mech. Phys. Solids* 48, 867 (2000).
17. Z.C. Olek, *The Finite Element Method for Solid and Structural Mechanics* (Boston: Butterworth-Heinemann, 2005).
18. V.N. Kaliakin, *Introduction to Approximate Solution Techniques, Numerical Modeling, and Finite Element Methods* (New York: Marcel Dekker, 2002).
19. F. Ren, E.D. Case, E.J. Timm, and H.J. Schock, *J. Alloys Compd.* 455, 340 (2008).
20. J.B. Wachtman, W.R. Cannon, and M.J. Matthewson, *Mechanical Properties of Ceramics* (New York: Wiley, 2009).
21. Z.A. Munir, U. Anselmi-Tamburini, and M. Ohyanagi, *J. Mater. Sci.* 41, 763 (2006).
22. I. Berkun, S.N. Demlow, N. Suwanmonkha, T.P. Hogan, and T.A. Grotjohn, *2012 MRS Fall Meeting Proceedings*, (Boston, MA, 2012).
23. O.L. Anderson, *J. Phys. Chem. Solids* 24, 909 (1963).
24. J.L.S.A. Migliori, *Resonant Ultrasound Spectroscopy: Applications to Physics, Materials Measurements, and Nondestructive Evaluation* (New York: Academic, 1997).
25. J.E. Ni, E.D. Case, K.N. Khabir, R.C. Stewart, C.-I. Wu, T.P. Hogan, E.J. Timm, S.N. Girard, and M.G. Kanatzidis, *Mater. Sci. Eng. B* 170, 58 (2010).
26. R.D. Schmidt, J.E. Ni, E.D. Case, J.S. Sakamoto, D.C. Kleinow, B.L. Wing, R.C. Stewart, and E.J. Timm, *J. Alloys Compd.* 504, 303 (2010).
27. R.D. Schmidt, E.D. Case, J.E. Ni, J.S. Sakamoto, R.M. Trejo, and E. Lara-Curzio, *Philos. Mag.* 92, 727 (2012).
28. L.D. Landau and E.M. Lifshitz, *Statistical Physics, Part 1*, 3rd ed. (Oxford: Pergamon, 1980).
29. M.I. Fedorov, V.K. Zaitsev, and M. V. Vedernikov, *ICT '06. 25th International Conference on Thermoelectrics* (2006), p. 111.
30. G.N. Isachenko, V.K. Zaĭtsev, M.I. Fedorov, A.T. Burkov, E.A. Gurieva, P.P. Konstantinov, and M.V. Vedernikov, *Phys. Solid State* 51, 1796 (2009).
31. G.D. Mahan, *Solid State Physics*, ed. E. Henry and S. Frans (Edinburgh: Academic, 1997), .
32. M.I. Fedorov, D.A. Pshenay-Severin, V.K. Zaitsev, S. Sano and M.V. Vedernikov, *Twenty-second International Conference on Thermoelectrics*, (2003).
33. M.I. Fedorov, *The 5th European Conference on Thermoelectrics*, (Odessa House of Scientists, Odessa, Ukraine, 2007).
34. G.A. Slack and M.A. Hussain, *J. Appl. Phys.* 70, 25 (1991).
35. T. Dasgupta, C. Stiewe, R. Hassdorf, A.J. Zhou, L. Boettcher, and E. Mueller, *Phys. Rev. B* 83, 235207 (2011).
36. Z. Du, T. Zhu, Y. Chen, J. He, H. Gao, G. Jiang, T.M. Tritt, and X. Zhao, *J. Mater. Chem.* 22, 6838 (2012).

37. R. Franz and G. Wiedemann, *Annalen der Phys.* 165, 497 (1853).
38. R.W. Keyes, *Phys. Rev.* 115, 564 (1959).
39. J. Tobola, S. Kaprzyk, and H. Scherrer, *J. Electron. Mater.* 39, 2064 (2010).
40. N.F. Mottt and E.A. Davis, *Electronic Processes in Non-crystalline Materials* (Oxford: Clarendon, 1971).
41. V. Milekhine, M.I. Onsøien, J.K. Solberg, and T. Skaland, *Intermetallics* 10, 743 (2002).
42. R.D. Schmidt, E.D. Case, J. Giles III, J.E. Ni, and T.P. Hogan, *J. Electron. Mater.* 41, 1210 (2012).
43. Z.W. Huang, Y.H. Zhao, H. Hou, and P.D. Han, *Phys. B* 407, 1075 (2012).
44. W.B. Whitten, P.L. Chung, and G.C. Danielson, *J. Phys. Chem. Solids* 26, 49 (1965).
45. F. Ren, E.D. Case, E.J. Timm, and H.J. Schock, *Philos. Mag.* 87, 4907 (2007).
46. G.H. Li, H.S. Gill, and R.A. Varin, *Metall. Trans. A* 24, 2383 (1993).
47. B. Kim, J. Jeon, K. Park, B. Park, Y. Park, and I. Park, *Arch. Mater. Sci. Eng.* 94, 94 (2008).
48. F. Ren, B.D. Hall, J.E. Ni, E.D. Case, J. Sootsman, M.G. Kanatzidis, E. Lara-Curzio, R.M. Trejo, and E.J. Timm, *Mater. Res. Soc. Symp. Proc.* 1044, 121 (2008).
49. L. Zhang, G. Rogl, A. Grytsiv, S. Puchegger, J. Koppensteiner, F. Spieckermann, H. Kabelka, M. Reinecker, P. Rogl, W. Schranz, M. Zehetbauer, and M.A. Carpenter, *Mater. Sci. Eng. B* 170, 26 (2010).
50. X. Fan, E.D. Case, X. Lu, and D.T. Morelli, *J. Mater. Sci.* 48, 7540 (2013).
51. F. Ren, E.D. Case, J.R. Sootsman, M.G. Kanatzidis, H. Kong, C. Uher, E. Lara-Curzio, and R.M. Trejo, *Acta Mater.* 56, 5954 (2008).
52. R.D. Schmidt, E.D. Case, G.J. Lehr, and D.T. Morelli, *Intermetallics* 35, 15 (2013).
53. J.B. Wachtman Jr, W.E. Tefft, D.G. Lam Jr, and C.S. Apstein, *Phys. Rev.* 122, 1754 (1961).
54. Y.P. Varshni, *Phys. Rev. B* 2, 3952 (1970).
55. J.M. Jackson, S.V. Sinogeikin, and J.D. Bass, *Phys. Earth Planet. Inter.* 161, 1 (2007).
56. L.C. Davis, W.B. Whitten, and G.C. Danielson, *J. Phys. Chem. Solids* 28, 439 (1967).